

DOI: 10.1002/((please add manuscript number))

Article type: Full Paper

Proof of concept studies directed towards the formation of metallic Ag nanostructures from Ag₃PO₄ induced by electron beam and femtosecond laser.

*Msc. Clayane Carvalho dos Santos^a, Msc. Marcelo de Assis^a, Dr. Thales Rafael Machado^a, Dr. Paula Fabiana dos Santos Pereira^a, Dr. Gladys Minguez-Vega^b, Dr. Eloisa Cordoncillo^c, Dr. Hector Beltran-Mir^c, Dr. Carlos Doñate-Buendía^b, Dr. Juan Andrés^{*d} and Dr. Elson Longo^a*

^aCDMF, Universidade Federal de São Carlos (UFSCar), P.O. Box 676, CEP, 13565-905 São Carlos-SP, Brazil.

^bGROC•UJI, Institut de Noves Tecnologies de l'imatge (INIT, University Jaume I (UJI), Castelló 12071, Spain.

^cDepartment of Inorganic and Organic Chemistry, University Jaume I (UJI), Castelló 12071, Spain.

^dDepartment of Analytical and Physical Chemistry, University Jaume I (UJI), Castelló 12071, Spain.

*E-mail: andres@qfa.uji.es

Prof^o Dr. Juan Andrés

Keywords: Ag₃PO₄, femtosecond laser, electron beam, Ag nanoparticles

In this work, for the first time, the instantaneous nucleation and growth processes of Ag nanoparticles on Ag₃PO₄ mediated by femtosecond laser pulses are reported and analyzed. The investigated samples were pure Ag₃PO₄ sample, electron irradiated Ag₃PO₄ sample, and laser irradiated sample. Complete characterization of the samples is performed using X-ray diffraction (XRD), Rietveld refinements, field emission scanning electron microscopy, and energy dispersive spectroscopy (EDS). XRD confirmed that the irradiated surface layer remains crystalline, and according to EDS analysis, the surface particles are composed

primarily of Ag nanoparticles. This method not only offers a one-step route to synthesize Ag nanoparticles using laser-assisted irradiation with particle size control, but also reports a complex process involving the formation and subsequent growth of Ag nanoparticles through an unexpected additive-free in situ fabrication process.

Introduction

The properties derived from the interaction of electrons/waves with matter have a key role in modern science and engineering. Energetic particle and/or electromagnetic interactions with solid materials have been studied for several decades, and the characterization of structure or property responses to these stimuli from the surrounding environment at the atomic scale have a key role in the understanding and rationalization of the structure–property–function relationship.^[1–2] Electron microscopy and laser techniques are based on these interactions. Further, the analysis of the scattered electrons and radiation after propagation through a specimen provides information regarding the structural and electronic properties of the sample. Conventional microstructure characterization of nanomaterials relies heavily on electron microscopy, where high-energy electrons transmit through the specimen and provide useful information at the nanometer and sub-nanometer levels of the samples based on a variety of electron–solid interactions. In the past decade, the advancement of technology associated with transmission electron microscopy has enabled direct observations of the growth process of nanostructured materials at high spatial and temporal resolutions.^[2–4] The interaction of femtosecond (fs) laser radiation with matter has been extensively studied and practically utilized for surface manipulation at the micro and nanoscale levels, having a critical role in material processing at the micro–nano-scale.^[5–13] In this context, Tan *et al.*^[14] presented a critical overview of the current state of the art in studying different fs laser-

induced phenomena in transparent materials including their physical and chemical mechanisms, applications and limitations, and future research trends. Although, these topics attract significant interest and demonstrate considerable potential for many applications, the phenomenology of these processes is complicated. Moreover, fundamental questions concerning the corresponding mechanisms continue to be debated and must be studied in detail.

Our research group, using a joint combination of experimental and theoretical studies, has conducted studies for understanding the formation mechanism of Ag nanoparticles (NPs)^[15–16] provoked by the exposure to electron beams of an electronic microscope on the surfaces of several Ag-based materials such as α -Ag₂WO₄,^[17–23] β -Ag₂WO₄,^[24–25] γ -Ag₂WO₄,^[26] β -Ag₂MoO₄,^[27–28] Ag₂CrO₄,^[29] AgVO₃,^[30] Ag₂V₂O₇,^[31] and Ag₃PO₄ crystals.^[32] Furthermore, we have reported four new phenomena provoked by fs laser irradiation: i) the scale-up of the formation of Ag NPs on α -Ag₂WO₄ with bactericidal properties,^[17] ii) the synthesis of metallic Bi NPs with coexisting crystallographic structures (rhombohedral, monoclinic, and cubic) on NaBiO₃,^[33] iii) the formation of In NPs on InP,^[34] and iv) the synthesis of Ag–Bi nanoalloys from inorganic oxide Ag₂WO₄ and NaBiO₃ target.^[35] Both fs and electron beam irradiation strategies allow us to obtain Ag NPs with interesting technological applications such as photoluminescent and bactericide materials.

A hybrid heterostructure formed by Ag NPs and Ag₃PO₄, Ag/Ag₃PO₄, was previously successfully synthesized and its application as a highly efficient and stable plasmonic photocatalyst validated.^[36–42] In this context, recently we reported and analyzed the formation of Ag nanostructures on Ag₃PO₄ induced by electron beam irradiation.^[32] Herein, inspired and as a continuation of these previous works, we report a systemic investigation of this phenomena and demonstrate a growth of Ag NPs on a surface of Ag₃PO₄ induced by fs laser

irradiation. The focus of this paper is three-fold: i) to report, for first time, the instantaneous nucleation and growth processes of Ag NPs on Ag_3PO_4 mediated by fs laser pulses; ii) to investigate samples that were pure Ag_3PO_4 (pAP), electron irradiated Ag_3PO_4 (eAP), and laser irradiated (lAP), iii) to compare this phenomena with previous observations where these processes that occur on Ag_3PO_4 are driven by an accelerated electron beam from an electronic microscope under high vacuum, and iv) to gain an improved understanding of this phenomenon and allow a finer control to future technological applications. Experimental techniques such as energy-dispersive X-ray spectroscopy (EDS) and transmission electron microscopy (TEM) with a high-angle annular dark field (HAADF) provide a valuable probe into the relationship between atomic-scale structural and electronic perturbations produced by fs laser pulses and electron beam material modification.

Results and discussion

Figure 1 displays the X-ray diffraction (XRD) patterns of the prepared samples. The diffraction peaks are all in agreement with the results reported in Inorganic Crystal Structure Data (ICSD) No. 1530, which are related to Ag_3PO_4 phase with a body-centered cubic structure (space group P-43n).^[32,44] No secondary phases were observed, even after the electron or laser irradiation. The narrow profiles of the diffraction peaks are related to a long-range structural ordering in these samples. The pAP and eAP XRD patterns are similar; the principal differences are observed in the lAP sample. In this specific case, the XRD pattern is less resolved and certain diffraction peaks no longer appear, such as the ones referred to as the (220), (411), (332), (422), and (510) peaks. Thus, in the lAP sample, laser irradiation induces a higher structural disorder at the long-range of the Ag_3PO_4 crystalline structure.. An analysis of the full width at half maximum (FWHM) of the most intense peak of the XRD patterns

related to plane (210) was performed to understand the degree of order/disorder among the samples at long range. The pAP sample had an FWHM of approximately 0.07° , causing this value to increase with different types of irradiation; the value was 0.016° for eAP and 0.025° for lAP. It was determined that when Ag_3PO_4 is subjected to fs laser/electron beam irradiation, a higher degree of disorder is added to the new material, caused by distortions in the crystal lattice of the Ag_3PO_4 .

<Figure 1>

Rietveld refinements [45] were employed to understand the differences in the structural arrangements of the prepared samples. In this work, the refinements were performed through the general structure analysis program (GSAS),^[46] assuming the spatial groups $P-43n$ for the cubic structure of the centered body of Ag_3PO_4 and adjusted to ICSD No. 1530.^[32] The plots of the refinements in Figure S1 in the supplementary material are in perfect agreement with the XRD patterns presented in Figure 1. Table 1 lists the fitting parameters (R_{wp} , R_p , R_{bragg} , χ^2), which revealed an acceptable adjust between the theoretical and observed XRD patterns. The results obtained from the refinement revealed similar lattice parameters for all samples as indicated in **Table 1**. However, the volume of the unit cell linearly decreases from the microcrystalline pAP and eAP, and thereafter from the lAP, where the results indicate a small degree of distortion in the short distance for the tetrahedral $[\text{AgO}_4]$ cluster with values of 93.54 , 93.61 , and 93.69° , respectively. This could be because the structure underwent a process of cell contraction, possibly forming a high density of Ag vacancies (VAg). The schematic representation of the unit cell of cubic lAP is illustrated in **Figure 2**.

<Figure 2>

<Table 1>

Raman spectroscopy was performed as a complementary technique to XRD to evaluate the order/disorder of the short-range. **Figure 3** displays the Raman spectra obtained at room temperature for the pAP, eAP, and lAP samples. According to the analysis derived from the group theory, Ag_3PO_4 exhibits 18 active modes in the Raman spectrum, corresponding to $\Gamma=2A_1+4E+12T_2$.^[32, 47] The bands at 77 and 223 cm^{-1} are associated with external translational and rotation modes associated with the $[\text{PO}_4]$ clusters. The bending vibration modes related to the $[\text{PO}_4]$ group were found at 406 and 551 cm^{-1} . The band at 709 cm^{-1} corresponds to symmetrical stretching vibrations of P-O-P linkages in the $[\text{PO}_4]$ clusters. The band located at 908 cm^{-1} is related to the symmetrical stretching vibrations of $[\text{PO}_4]$, and asymmetrical stretching was verified at 951 and 1001 cm^{-1} .^[32, 48-51]

In the Raman spectra displayed in Figure 3, changes in the intensity of the vibrational modes related to the $[\text{PO}_4]$ clusters such as those at 223, 551, 908, 951, and 1001 cm^{-1} can be observed. This behavior is more pronounced for lAP, indicating an important short-range disorder in this sample. Hence, a higher concentration of structural defects than pAP and eAP samples is provoked by the interaction of the fs laser.

<Figure 3>

The analysis of the Raman spectra and Rietveld refinements indicates that both $[\text{PO}_4]$ and $[\text{AgO}_4]$ clusters are distorted with changes with respect to their equilibrium values for the O-P and O-Ag bond distances, and the O-P-O and O-Ag-O bond angles. One $[\text{PO}_4]$ cluster and three $[\text{AgO}_4]$ clusters are joined through the corner O anion. The Ag-O bonds of the $[\text{AgO}_4]$ clusters are more labile than the P-O bonds of the $[\text{PO}_4]$ clusters. Therefore, $[\text{PO}_4]$ clusters are more difficult to perturb by an external stimulus, making the $[\text{AgO}_4]$ clusters more susceptible to interact with incoming electrons/photons.

X-ray Photoelectron Spectroscopy (XPS) measurements were performed to compare the pAP, eAP, and lAP samples. The XPS spectrum displayed in **Figure 4a** indicates the presence of Ag, P, and O peaks, confirming the high degree of purity of the samples. Peaks related to C were also observed, which are related to the carbon pollution from the XPS instrument itself.^[52–53] The high resolution XPS spectra in Figures 4b–d indicate two peaks with binding energies of approximately 367 eV and 373 eV, attributed to Ag 3d_{5/2} and Ag 3d_{3/2} orbitals, respectively.^[53–54] Moreover, each of these peaks could be fitted in two separate components, indicating the presence of Ag in varied valences. These asymmetric peaks were fitted as described in Figures 4b–d at 367.13/367.97 eV for Ag 3d_{5/2} and at 373.14/373.98 eV for Ag 3d_{3/2}. The high intensity peaks at 367.13 and 373.14 eV correspond to Ag⁺ ions, whereas the low intensity peaks at 367.97 and 373.98 eV are associated to metallic Ag.^[55–60]

<Figure 4>

In the formed Ag/Ag₃PO₄ heterostructure, the amount of metal Ag in the microcrystals samples is considerably variable, i.e., the metallic Ag content for the pAP, eAP, and lAP samples was calculated, considering a mean area of metallic silver on the surface of the samples, to be 18.86%, 23.12%, and 19.85%, respectively. A higher metal Ag⁰ content is observed on the surface of the eAP sample, which is possibly associated with the larger amount fixed to the surface of the microcrystal; this is confirmed by the measurements of the scanning microscopy.

To examine the chemical characteristics of the P 2p bond, we verified the high-resolution P 2p level spectra for all the samples analyzed. Figure S2 in the supplementary material clearly indicates the spin-orbital division between the P2p_{1/2} and P2p_{3/2} peaks in the P 2p core-level spectra, which corresponds to the characteristic binding energy of the P⁵⁺ oxidation state in Ag₃PO₄; the samples do not indicate significant differences.

FE-SEM images of pAP, eAP, and lAP exposure are displayed in **Figure 5**. In all the samples, irregular spherical microparticles with large size dispersion and aggregates can be observed. The particle dimensions for pAP, eAP, and lAP are 712, 468, and 432 nm, respectively. Further, it was possible to observe the nucleation and growth processes of metallic Ag NPs on the Ag_3PO_4 microcrystals surfaces. These processes occur via diffusion of the Ag^+ species from their positions at the crystalline lattice corresponding to the $[\text{AgO}_4]$ clusters to the Ag_3PO_4 surface, with subsequent reduction to Ag^0 . Both migration and reduction processes of the Ag^+ species are provoked by the electron beam and laser irradiations. The metallic Ag nanoparticles on the eAP sample are predominantly rod-shaped, whereas the majority of the Ag nanoparticles on the lAP sample are composed of irregular spheres.

<Figure 5>

The samples, pAP, eAP, and lAP, were also characterized by TEM. **Figures 6a–c** display the obtained TEM images at low magnification. As in the case of Figure 5, the nucleation of Ag nanoparticles on the surface of the samples was also observed for eAP (nanorods) (Figure 6b) and lAP (irregular nanospheres) (Figure 6c). Moreover, owing to the high energy of the TEM analysis, the pAP also presented the initial stage of growth of Ag nanoparticles, which was included for comparison. To confirm this behavior of the nucleation of the Ag nanostructures, EDS analysis was also performed in two distinct regions of each image (Ag_3PO_4 and Ag nanoparticles). Region 1 was selected in the center of the Ag_3PO_4 microparticle; Region 2 was selected in the Ag NPs. The results confirmed the presence of Ag, P, and O in Region 1 and predominantly Ag in Region 2, confirming the presence of metallic Ag in all samples. Cu and C refer to the sample port grid.

<Figure 6>

Different morphologies of Ag NPs were observed for both samples, as indicated in **Figure 7a-b**. The eAP sample presents a 1D nanostructure in the form of nanorods, Figure 7a, whereas the IAP sample presents a zero-dimensional nanostructure in the irregular spherical shape, Figure 7b. This difference in morphology of Ag nanoparticles is caused by the differences in the formation process, leading to different time, temperature and pressure conditions. For fs laser irradiation, the sample can reach a pressure around 1010 Pa and a temperature of 1000K,^[17] thus causing the formation of a large number of confined photons in a small area. Moreover, when irradiated with fs pulses the sample is in the steady state, that is, it does not present vibrational and rotational movements, since these occur in the second peak scale, which makes it difficult to follow the dynamic process of particle nucleation.^[15, 35]

<Figure 7>

These Ag nanoparticles were analyzed using HR-TEM in order to find the crystalline planes. The surface of these nanoparticles with light edges indicates a monocrystalline nature. This is confirmed by the reciprocal distances, with the strongest face cubic metallic Ag nanoparticles characterized by a (111) plane with an interplanar distance of 0.23 nm (Figure 7), corresponding to PDF 89-3722 in the JCPDS (Joint Committee on Powder Diffraction Standards).^[32]

In this part of the study, the initially formed Ag/Ag₃PO₄ composite of eAP and IAP samples were irradiated by a gradual converging electron beam. For this experiment, the electron beam of the TEM was condensed over these particles to increase the current density and to promote structural transformations. **Figures 8a–b** display the selected regions. An analysis of the results verifies that small and well-dispersed nanoparticles were formed near the initial Ag nanorod (eAP) or Ag irregular spheres (IAP) a few nanometers away from the initial Ag NPs. The HR-TEM images in the insets of both figures demonstrate an interplanar

distance of 0.23 nm for these particles, which can be associated to the (111) plane of cubic metallic Ag.^[61] Thus, the exposure of a secondary electron beam from TEM leads to the growth of metallic Ag from the initial particles obtained in the eAP and IAP samples. Figures 8a–b indicates that the dimensions of these particles are in the range of 2.26 and 3.36nm for samples eAP and IAP, respectively. The Ag cations migrate from the matrix to the surface, resulting in structural and morphological modifications with the appearance of Ag vacancies.^[32]

<Figure 8>

The above results can be viewed as an example of the electron beam-induced fragmentation process of the initial Ag particles by exposure to a condensed electron beam. This is a well-known process that results from the transfer of thermal energy and electric charge.^[62–63] This phenomenon occurs in metallic samples that can melt and collapse into spherical units as the irradiating current density increases. The newly formed Ag NPs are expelled and “fly” in the carbon grid for several nanometers, as observed in the eAP and IAP samples.

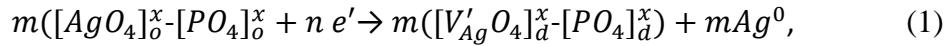
Figure 9 presents the proposed growth mechanisms of the Ag NPs. The structure was irradiated with different energy levels, originating two morphologies associated to different metal nanoparticles, a nanobastones morphology, related to electron irradiation, and irregular spheres for fs laser irradiation.

<Figure 9>

The universality of Ag NPs generation through electron beam and/or fs laser pulses naturally indicates the existence of a **common mechanism and in both cases**, the interaction of the laser/electron beam on the Ag_3PO_4 provokes the reduction of Ag^+ ion to form metal Ag^0 .

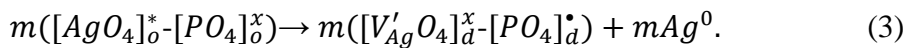
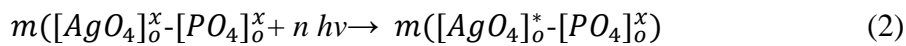
When the surface of the Ag_3PO_4 semiconductor is irradiated with an fs laser, the electrons of the valence band are excited to the conduction band. Because the electrons provide the bonding forces that hold atoms together in the lattice, if their distribution within the material changes significantly, the bonding forces can also change. At the local level, the multiphoton absorption of light leads to the excitation of the constituent clusters; $[\text{PO}_4]$ and $[\text{AgO}_4]$ are now located in an excited state where the Ag-O chemical bond no longer exists. This results in the formation of a plasma plume leading to the appearance of structural and electronic surface disorder. In the plasma, there are non-stoichiometric nanoparticles of Ag_3PO_4 and Ag metal. Then, the formation of metallic Ag and Ag vacancies occurs on the surface of the semiconductor.

The proposed mechanism for the formation of metallic Ag NPs on the surface of Ag_3PO_4 provoked by an electron beam is presented in Figure 9, and can be described by Eqs. (1)–(3):



where n is number of electron or photons involved in the process, m is the number of clusters involved in the process, $[\text{AgO}_4]$ and $[\text{PO}_4]$ are the forming clusters of Ag_3PO_4 , $[\text{VAgO}_4]$ refers to silver vacancy, and the sub-indices o and d refer to cluster order/disorder.

Equations (2) and (3) are associated with the photon interaction on Ag_3PO_4 :



The agglomeration processes of neutral Ag atoms caused by the electron and laser irradiation are summarized in Eq. (4).



When the crystal of pAP is electron-irradiated, there is a reduction of Ag cations along an ordered movement from the bulk to the surface of the crystal. This promotes the formation of metallic Ag on its surface, which depends on the irradiation time and density of the injected electrons. Conversely, laser irradiation promotes an instantaneous Ag growth. Owing to the ultrashort pulse duration, fs scale, the pAP crystal loses symmetry and the metallic Ag NPs grows rapidly in a disorderly manner. These two experiments prove that electron and photons produce the same effect over the irradiated material. In this manner, the photo reduction and electron reduction effects, followed by an atomic displacement and Ag crystallization in the two experiments on the surface of a semiconductor crystal can be observed, see Figure o9b. The valence electrons responsible for the chemical bonds that hold the solids together are thus easily removed during the laser ablation process. This causes a mutually repulsive state between the atoms whose chemical bonds are broken, and the agglomerate explodes owing to mutual electrostatic repulsion of the ions.

Experimental Section

Synthesis: *Synthesis of Ag_3PO_4 microcrystals:* The methodology employed for the synthesis of the Ag_3PO_4 microcrystals was a simple chemical precipitation at room temperature, as described in detail previously.^[32] Briefly, 75 mL of an aqueous solution containing 3 mmol of $AgNO_3$ (99.8%, Vetec) and 25 mL of an aqueous solution containing 1 mmol of NaH_2PO_4 (98.6%, J.T.Baker) were prepared. Both solutions were quickly mixed in constant agitation, promoting the instantaneous formation of yellow Ag_3PO_4 precipitate. The mixture was then stirred for 10 min. The precipitates obtained were washed several times with deionized water and centrifuged to remove the by-products formed during the reaction. The resulting powder

was dried at 60 °C for several hours under air atmosphere. The sample obtained in this procedure is referred to as the pAP.

Electron beam irradiation of Ag_3PO_4 : A Carl Zeiss DSM940A scanning electron microscope (Germany) with an accelerating voltage of 30 kV was used to irradiate the sample with electrons. In this procedure, the pAP powder was placed in a cylindrical sample holder. The electron beam exposure time was fixed at 5 min. The sample obtained here is referred to as the eAP.

Femtosecond laser irradiation of Ag_3PO_4 : The fs laser irradiation scheme is displayed in **Figure 10**. The pure Ag_3PO_4 (pAP) sample was irradiated with a Ti:sapphire laser (Femtopower Compact Pro, Femto Lasers) emitting 30 fs pulses, FWHM, with a central wavelength of 800 nm and a repetition rate of 1 kHz. An iris was used to obtain a 6 mm laser beam that was focused on the surface of a powder target of Ag_3PO_4 using a 75 mm lens **which allows to obtain a focal spot in the processing plane with a diameter of about 21 μ m FWHM.** The pAP sample was placed at the bottom of a quartz cuvette attached to a two-dimensional motion-controlled stage moving at a constant speed of 0.5mm/s. To ensure that the laser interacted with the entire sample, the irradiation process was repeated four times after stirring the sample each time. A mean power of **10, 80 and 200 Mw**, Figure S3 in the supplementary material, was used to irradiate the sample. **These provides a fluence over the sample of about 3, 24 and 60 J/cm^2 , respectively. Experimentally, we observed that the results of the synthesized nanoparticles with these different laser parameters were similar. Previously, we show that the optimal conditions for the irradiation of semiconductors by femtosecond lasers result when the sample is irradiated with a mean power of 200 mW.**^[17,33] Finally, to ensure that the pulse duration of the laser at the focal plane was 30 fs, a user-adjustable post-compression stage based on a pair of fused silica Brewster prisms was employed to

compensate for the dispersion in the beam delivery path. The sample obtained in this procedure is referred to as the fs IAP. **Although for comparison with our previous papers we employ a femtosecond laser,^[17,33-35] further studies can be conducted in order to elucidate if it is possible the formation of metallic Ag fby irradiation of pAP with other kind of lasers, as it happens in other Ag-containing compounds^[64,65].**

<Figure 10>

Characterization: The pAP, eAP, and IAP samples were structurally characterized by powder XRD using a Rigaku D/Max-2500PC diffractometer (Japan) with *Cu-K α* radiation ($\lambda = 0.15406$ nm). Data were collected in a 2θ range of 10–110° using a step scan rate and step size of 1°/min and 0.02°. Raman spectroscopy was performed using a Horiba Jobin-Yvon IHR550 (Japan) spectrometer coupled to a CCD detector and a Melles Griot, United States laser (USA), operated at 633 nm. XPS was performed using a Scienta Omicron ESCA+ spectrometer with a high-performance hemispheric analyzer (EA 125) with monochromatic Al K α ($h\nu = 1486.6$ eV) radiation as the excitation source. The operating pressure in the ultrahigh vacuum chamber (UHV) during analysis was 2×10^{-9} mbar. Energy steps of 50 and 20 eV were used for the survey and high-resolution spectra, respectively. The binding energies of all elements were calibrated by referencing to the C 1s peak at 284.8 eV.

The morphological features of Ag₃PO₄ microparticles and the effect of electron beam and fs laser exposure on the growth mechanisms of metallic Ag NPs was first examined by field emission scanning electron microscopy (FE-SEM) with a Carl Zeiss Supra 35VP (Germany) microscope operating at 5 kV. In this procedure, the micrographs were recorded as soon as possible to avoid influence of the electron beam during the FE-SEM characterization of the prepared samples. TEM and high-resolution TEM (HRTEM) micrographs, as well as

EDS analysis were performed with an FEI TECNAI F20 (Netherlands) microscope operating at 200 kV. HAADF image and EDS mapping were recorded in scanning transmission mode. The samples were prepared by depositing small amounts of the powders directly onto holed carbon-coated Cu grids to capture information regarding the nucleation and growth mechanisms of the metallic Ag.

Supporting Information

Supporting Information is available from the Wiley Online Library or from the author.

Acknowledgments

The authors acknowledge the financial support of agencies: Coordenação de Aperfeiçoamento de Pessoal de Nível Superior – Brazil (CAPES) – Finance code 001 – PNPd program, FINEP, FAPESP (2013/07296-2, 2013/26671-9, 2014/14171-4), CNPq (166281/2017-4), IFMA - *Campus Açailândia*, Generalitat Valenciana for PrometeoII/ 2014/022, Prometeo/2016/079, ACOMP/2015/1202, Ministerio de Economía y Competitividad, projects CTQ2015-65207-P and FIS2016-75618-R and Universitat Jaume I” project No. UJI-B2016-25. The authors thanks to Enio Longo for the support with the scientific illustrations. We acknowledge to the Servei Central d'Instrumentació Científica for the use of the femtosecond laser facility.

Conflict of Interest

The authors declare no conflict of interest.

Keywords

Ag₃PO₄, femtosecond laser, electron beam, Ag nanoparticles

Received: ((will be filled in by the editorial staff))

Revised: ((will be filled in by the editorial staff))

Published online: ((will be filled in by the editorial staff))

References

- [1] A. Moliton, *Electromagnetism and Materials*. Springer, **2007**.
- [2] R. Ramachandramoorthy, R. Bernal, H.D. Espinosa, *ACS Nano*. **2015**, *9*, 4675.
- [3] J.M. Thomas, R.K. Leary, A.S. Eggeman, P.A. Midgley, *Chem. Phys. Lett.* **2015**, 103.
- [4] O. Ersen, I. Florea, C. Hirlimann, C. Pham-Huu, *Mater. Today*. **2015**, *18*, 395.
- [5] I.G. Gonzalez-Martinez, A. Bachmatiuk, V. Bezugly, J. Kunstmann, T. Gemming, Z. Liu, G. Cuniberti, M.H. Rummeli, *Nanoscale* **2016**, *8*, 11340.
- [6] W. Xiong, Y. Zhou, W. Hou, L. Jiang, M. Mahjouri-Samani, J. Park, X. He, Y. Gao, L. Fan, T. Baldacchini, J.F. Silvain, Y. Lu, *Front. Optoelectron.* **2015**, *8*, 351.
- [7] G. G. Rubio G, P. Díaz-Núñez, A. Rivera, A. Prada, G. Tardajos, G. J. Izquierdo, L. Bañares, P. Llombart, L. G. Macdowell, M. A. Palafox, L. M. Liz-Marzán, O. Peña-Rodríguez, A. Guerrero-Martínez¹, *Science* **2017**, *8*, 640.
- [8] L. Wang, Q. Li, H.Y. Wang, J.C. Huang, R. Zhang, Q.D. Chen, H.L. Xu, W. Han, Z.Z. Shao, H.B. Sun, *Light Sci. Appl.* **2015**, *4*, 1.
- [9] M. Haque, K.K.C. Lee, S. Ho, L.A. Fernandes, P.R. Herman, *Lab Chip*. **2014**, *14*, 3817.
- [10] A. Y. Vorobyev, C. Guo, *Laser Photonics Rev.* **2013**, *7*, 385.
- [11] J. Bonse, J. Krüger, S. Höhm, A. Rosenfeld, *J. Laser Appl.* **2012**, *24*, 042006.
- [12] J. Bonse, S. Höhm, S.V. Kirner, A. Rosenfeld, J. Krüger, *IEEE J. Sel. Top. Quantum Electron.* **2017**, *23*, 109.
- [13] R. Buividas, M. Mikutis, S. Juodkazis, *Prog. Quantum Electron.* **2014**, *38*, 119.
- [14] D. Tan, K.N. Sharafudeen, Y. Yue, J. Qiu, *Prog. Mater. Sci.* **2016**, *76*, 154.
- [15] J. Andrés, A. F. Gouveia, L. Gracia, E. Longo, G. M. Faccin, E. Z. Silva, D. H. Pereira, M. A. San-Miguel, *Int. J. Quantum chem.* **2018**, *118*, 25551.
- [16] G. M. Faccin, M. A. San-Miguel, J. Andrés, E. Longo, E. Z. Silva, *J Phys Chem C*. **2017**, *121*, 7030.
- [17] M. Assis, E. Cordoncillo, R. Torres-Mendieta, H. Beltrán-Mir, G. Mínguez-Vega, R.C. Oliveira, E.R. Leite, C.C. Foggi, C.E. Vergani, E. Longo, J. Andrés, *Sci Rep.* **2018**, *8*, 1.
- [18] V. M. Longo, C. C. De Foggi, M. M. Ferrer, A. F. Gouveia, R. S. André, W. Avansi, C. E. Vergani, A. L. Machado, J. Andrés, L. S. Cavalcante, A. C. Hernandez, E. Longo, *J. Phys. Chem. A*. **2014**, *118*, 5769.

- [19] E. Longo, D.P. Volanti, V.M. Longo, L. Gracia, I.C. Nogueira, M.A.P. Almdeira, A.N. Pinheiro, M.M. Ferrer, L.S. Cavalcante, J. Andrés, *J. Phys. Chem. C* **2014**, *118*, 1229.
- [20] M. A. San-Miguel, E. Z. da Silva, S. M. Zanetti, M. Cilense, M. T. Fabbro, L. Gracia, J. Andrés, E. Longo, *principles. Nanotechnol* , **2016**, *27*, 225703.
- [21] J. Andrés, L. Gracia, P. Gonzalez-Navarrete, V.M. Longo, W.J. Avansi, D.P. Volanti, M.M. Ferrer, P.S. Lemos, F.A. La Porta, A.C. Hernandez, E. Longo, *Sci. Rep.* **2014**, 5391.
- [22] W. S. Pereira, J. Andrés J, L.Gracia, M. A. San-Miguel, E. Z. Silva, E. Longo, V. M. Longo, *Phys. Chem. Chem. Phys.* **2015**, *17*, 5352.
- [23] E. Longo, L.S. Cavalcante, D.P. Volanti, A.F. Gouveia, V.M. Longo, J.A. Varela, M.O. Orlandi, J. Andrés, *Sci. Rep.* **2013**, *3*, 1676.
- [24] R.A. Roca, A.F. Gouveia, P.S. Lemos, L. Gracia, J. Andrés, E. Longo, *Inorg. Chem.* **2016**, *55*, 8661.
- [25] R. A. Roca, P. S. Lemos, J. Andrés, E. Longo, *Chem. Phys. Lett.* **2016**, *244*, 68.
- [26] R. A. Roca, P. S. Lemos, L.Gracia, J. Andrés, E. Longo, *R. Soc. Chem.* **2017**, *7*, 5610.
- [27] M.T. Fabbro, L. Gracia, G.S. Silva, L.P.S. Santos, J. Andrés, E. Cordoncillo, E. Longo, *J. Solid State Chem.* **2016**, *239*, 220.
- [28] J. Andres, M. M. Ferrer, L. Lourdes, A. Beltran, V. M. Longo, G. H. Cruvinel, R. L. Tranquilin, E. Longo, *Part Part Syst Charact.* **2015**, *32*, 646.
- [29] G.S. Silva, L. Gracia, M. T. Fabbro, L. P. S. Santos, Luis P.; H. Beltran-Mir, E. Cordoncillo, E. Longo, J. Andres, *Inorg. Chem.* **2016**, *55*, 8961.
- [30] R.C. de Oliveira, S.M. Zanetti, M. Assis, M. Penha, M. Mondego, M. Cilense, E. Longo, L.S. Cavalcante, *J. Am. Ceram. Soc.* **2017**, *100*, 2358.
- [31] R. C. Oliveira, C. C. Foggi, M. Mondego, M. D. S. Penha, M. Assis, F. M. Francisco, B. N. A. S. Pimentel, P.F. S. Pereira, C. E. Vergani, A. L. Machado, J. Andrés, L. Garcia, E. Longo, *ACS Appl Mater Interfaces.* **2017**, *9*, 11472.
- [32] G. Botelho, J. C. Sczancoski, J. Andres, L. Gracia, E. Longo, *J. Phys. Chem.* **2015**, *119*, 6293.
- [33] M. Assis, E. Cordoncillo, R. Torres-Mendieta, H. Beltran, G. Mínguez-Vega, A.F. Gouveia, E. R. Leite, J. Andrés, E. Longo, *Phys Chem Chem Phys.* **2018**, *20*, 13693.
- [34] M. Assis, N. G. Macedo, T. R. Machado, M. M. Ferrer, A. F. Gouveia, E. Cordoncillo, R. Torres-Mendieta, H. Beltrán-Mir, G. Mínguez-Vega, E.R. Leite, J. R. Sambrano, J. Andrés, E. Longo, *Part Part Syst Charact.* **2018**, *180037*, 1.
- [35] T. R. Machado, N. G. Macedo, M. Assis, C. Doñate-Buendia, G. Mínguez-Vega, Gladys, M. T. Teixeira, C.C. Foggi, C. E. Vergani, H. Beltrán-Mir, Héctor, J. Andrés, E. Cordoncillo, E. Longo, *ACS Omega.* **2018**, *3*, 9880.
- [36] Y. Liu, L. Fang, H. Lu, L. Liu, H. Wang H, C. Hu, *Catal. Commun.* **2012**, *17*, 200.

- [37] J. Yu, J. Yu, T. Ying, C. Cui, Y. Sun, X. Liu, *J Alloy Compd.* **2019**, 775, 225.
- [38] W. Teng, X. Li, Q. Zhao, J. Zhao, D. Zhang. *Appl Catal B-Environ.* **2012**, 125, 538.
- [39] M. A. Gondal, X. Chang, W. E. I. Sha, Z. H. Yamani, Q. Zhou, *J Colloid Interf Sci.* **2013**, 392, 325.
- [40] K. Huang, Y. Lv, W. Zhang, S. Sun, B. Yang, F. Chi, S. Ran, X. Liu, *Mater. Res. Lett.* **2015**, 18, 939.
- [41] Y. Bi, H. Hu, S. Ouyang, Z. Jiao, G. Lu, J. Ye, *Chem.Eur. J.* **2012**, 18, 14272.
- [42] T. Yana, W. Guan, Y. Xiao, J. Tiaa, Z. Qiao, H. Zhai, W. Li, J. Youa, *Appl Surf Sci.* **2017**, 391, 592.
- [43] W. Teng, X. Y. Li., Q. D. Zhao, J. J. Zhao, D. K. Zhang, *Appl Catal B-Environ.* **2012**, 125, 538.
- [44] J. J. Liu, X. L. Fu, S. F. Chen, Y. F. Zhu, J. J. Liu, X. L. Fu, S. F. Chen, Y. F. Zhu, *Appl. Phys. Lett.* **2011**, 99, 2011.
- [45] H. M. A Rietveld, *J. Appl. Crystallogr.* **1969**, 2, 65.
- [46] B. H Toby, *J. Appl. Crystallogr.* **2001**, 34, 210.
- [47] X. Q. Liu, W. J. Chen, H. Jiang, *Chem Eng J.* **2017**, 308, 889.
- [48] Q. Liang, Y. Shi, W. Ma, Z. Li, X. Yang, *Chem Chem Phys.* **2012**, 14, 15657.
- [49] P. Dong, Y. Wang, B. Cao, S. Xin, L. Guo, J. Zhang, F. Li, *Appl. Catal., B.* **2013**, 132, 44..
- [50] L.W. Cheng,; J. C. Tsai, T. Y. Huang, C. W. Huang, B. Unnikrishnan, Y.W. Lin, *Mater. Res. Express*, **2014**, 1, 1.
- [51] M. Mroczkowska, J. L. Nowinski, G. Z. Zukowska, A. Mroczkowska, J. E. Garbarczyk, M. Wasiucioneck, S. Gierlotka, *J. Power Sources*, **2007**, 173, 729.
- [52] W. Teng, X. Li, Q. Zhao, G. Chen, *J. Mater. Chem. A.* **2013**, 1, 9060.
- [53] D. Seo, J. C. Park, H. Song, *J. Am. Chem. Soc.* **2006**, 128, 14863.
- [54] P. Wang, B. Huang, Q. Zhang, X. Zhang, X. Qin, Y. Dai, J. Zhan, J. Yu, H. Liu, Z. Lou, *Chem. Eur. J.* **2010**, 16, 10042.
- [55] P. Dong, G. Hou, C. Liu, H. Tian, F. Xu, X. Xi, R. Shao, G.R. Patzke, *ed. Materials.* **2016**, 9, 968.
- [56] C.G. Kontoyannis, N.V. Vagenas, *Analyst.* **2000**, 125, 251.
- [57] T. Yan, W. Guan, J. Tian, P. Wang, B. Huang, *J. Alloys Compd.* **2016**, 680, 436.
- [58] J. Wan, E. Liu, J. Fan, X. Hu, L. Sun, C. Tang, Y. Yin, H. Li, Y. Hu, *Ceram. Int.* **2015**, 41, 6933.
- [59] H. Zhang, W. Geng, D. Ghen, X. Lv, J. Li, *Chem. Mater.* **2008**, 20, 6543.

- [60] L. Cai, X. Xiong, N. Liang, Q. Long, *Appl. Surf. Sci.* **2015**, 353, 939.
- [61] W. S. Pereira, J. C. Sczancoski, Y. Colmenares, V. Mastelaro, G. Botelho, T. Machado, E. R. Leite, E. Longo, *Appl. Surf. Sci.* **2018**, 440, 61.
- [62] J. M. P. Coelho, C. Silva, A. Ruivo, A. P. Matos, *Mater. Sci. Forum*, **2012**, 915, 730.
- [63] W. D. Pyrz, S. Park, T. Vogt, D. J. Buttrey, *J. Phys. Chem. C*. **2007**, 111, 10824.
- [64] E. K. Fields, Seymour Meyerson, *J. Org. Chem.*, **1976**, 41, 916.
- [65] H.-T. Chen, H.-L. Lin, C. Kuo and I.-G. Chen, *J. Mater. Chem. C*, **2016**, 4, 7675.

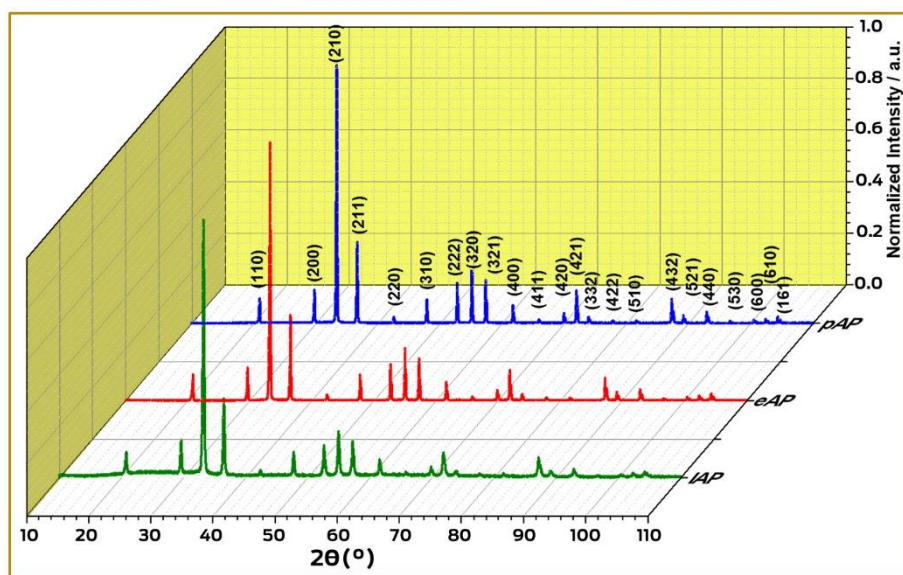


Figure 1. XRD patterns of Ag_3PO_4 microcrystals: pure (pAP) electron irradiation (eAP) and femtosecond laser irradiation (lAP)

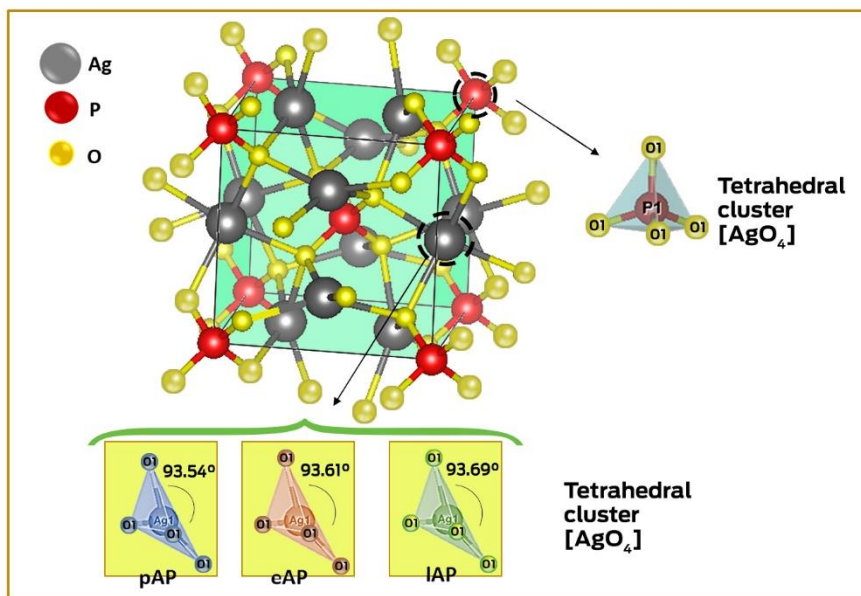


Figure 2. Schematic representation of the cubic body centered Ag_3PO_4 structure, illustrating $[\text{AgO}_4]$ and $[\text{PO}_4]$ clusters.

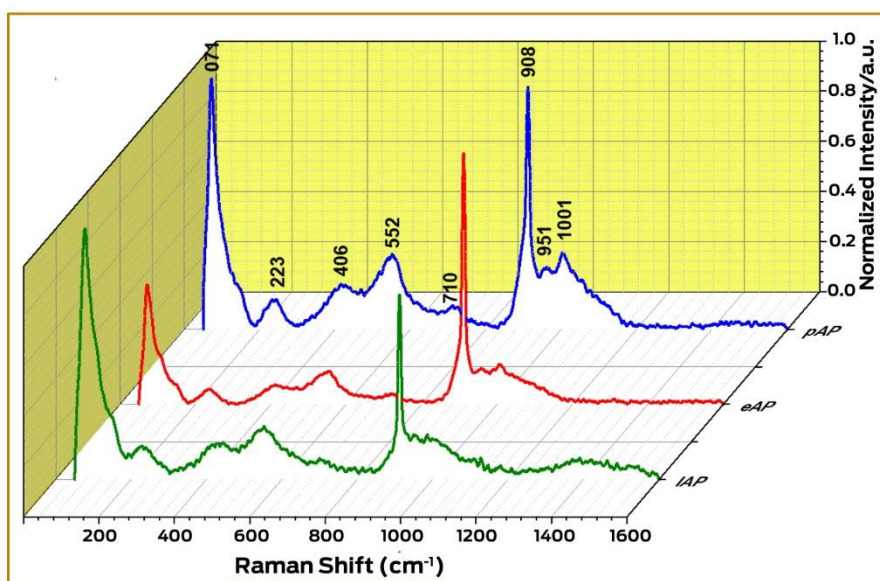


Figure 3. Micro-Raman of Ag_3PO_4 microcrystals: pure (pAP) electron irradiation (eAP) and femtosecond laser irradiation (IAP)

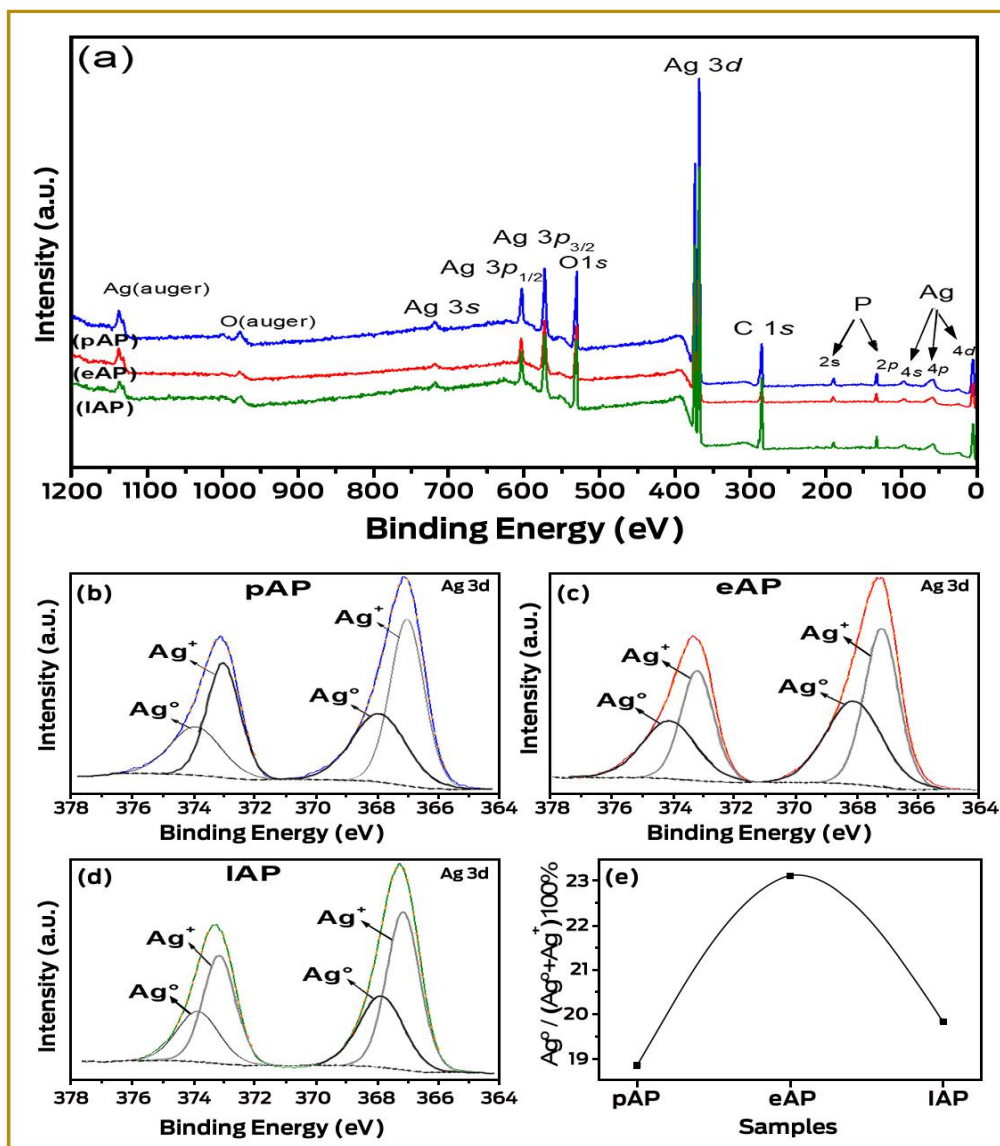


Figure 4. XPS survey spectrum of the samples microcrystals (a); High-resolution XPS spectra of Ag3d region of the samples pure (b), electron irradiation (c) and femtosecond laser irradiation (d); and the ratios of peak area attributed to Ag⁰ to the total area of all for these samples (e)

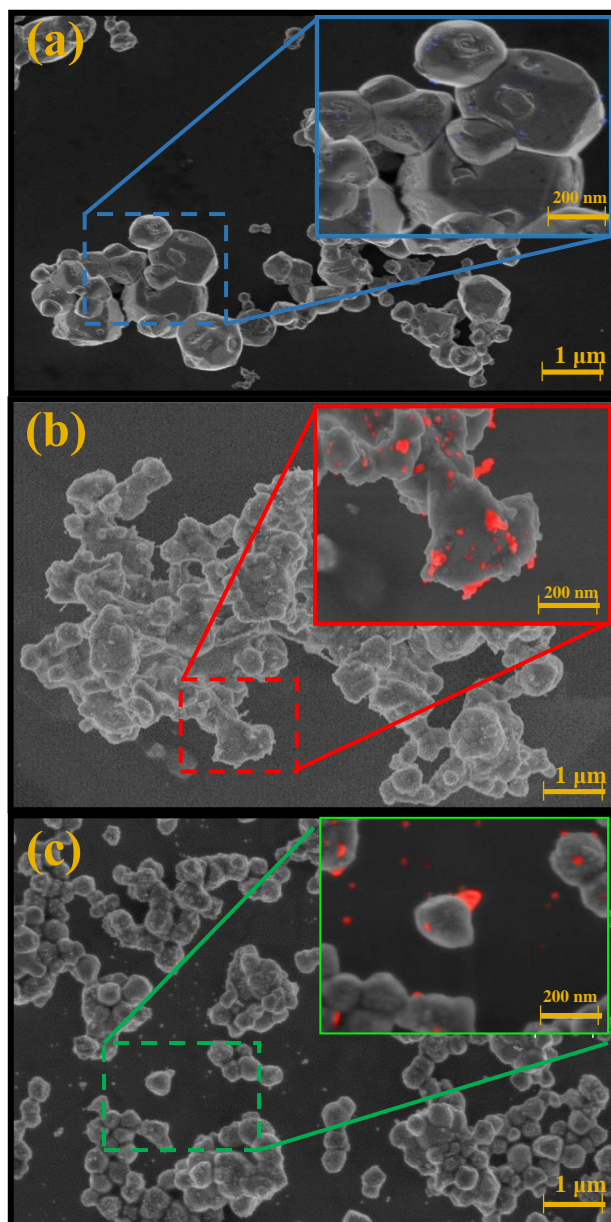


Figure 5. SEM images of Ag_3PO_4 microcrystals: pure (pAP) electron irradiation (eAP) and femtosecond laser irradiation (lAP). The Ag NPs are painted in red color.

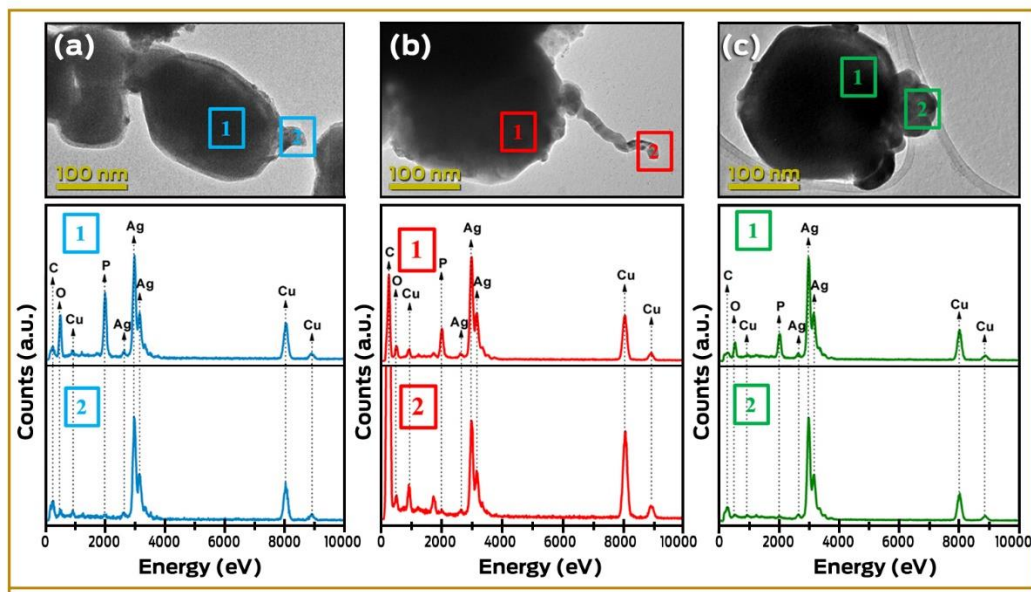


Figure 6. TEM of Ag_3PO_4 microcrystals: pure (pAP) electron irradiation (eAP) and femtosecond laser irradiation (IAP)

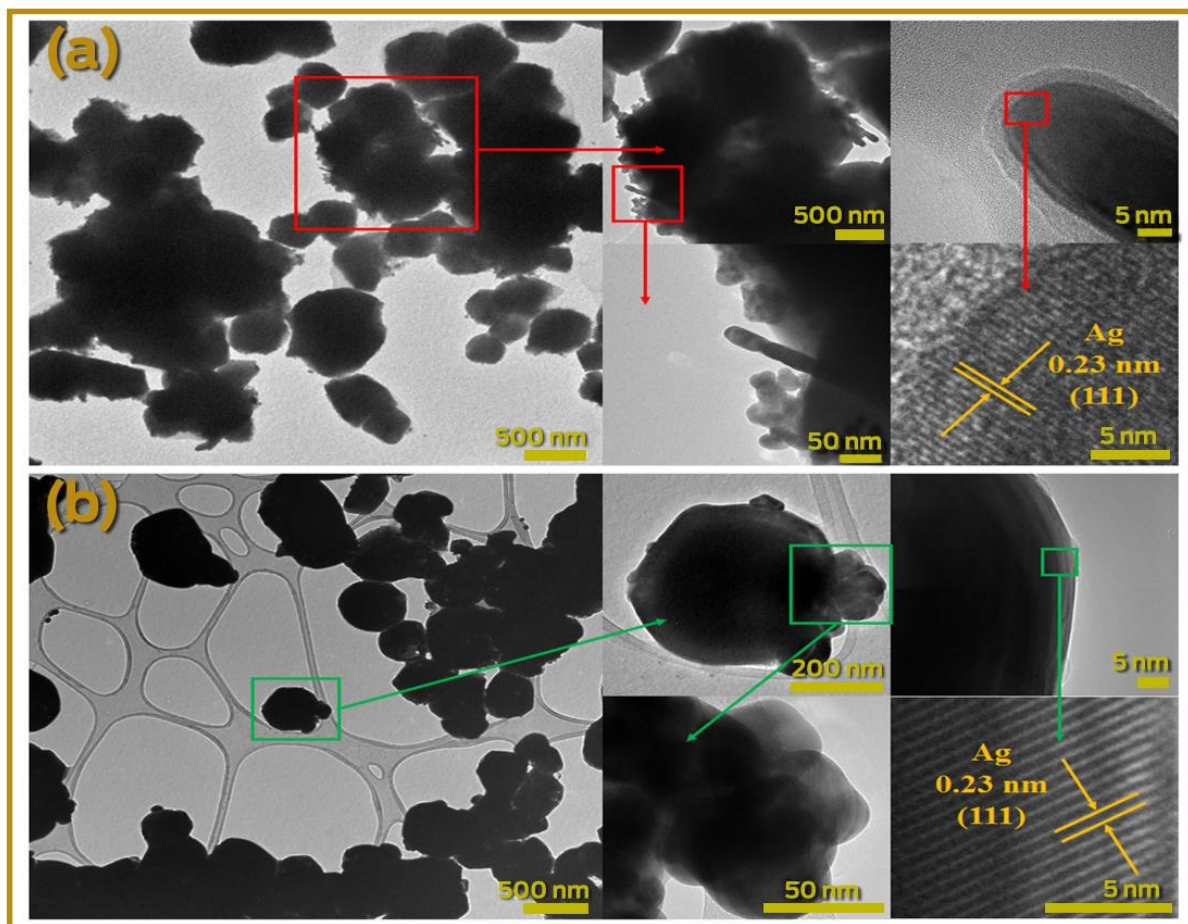


Figure 7. TEM micrographs at higher magnification of individual crystallites with: a) electron irradiation and b) femtosecond laser irradiation

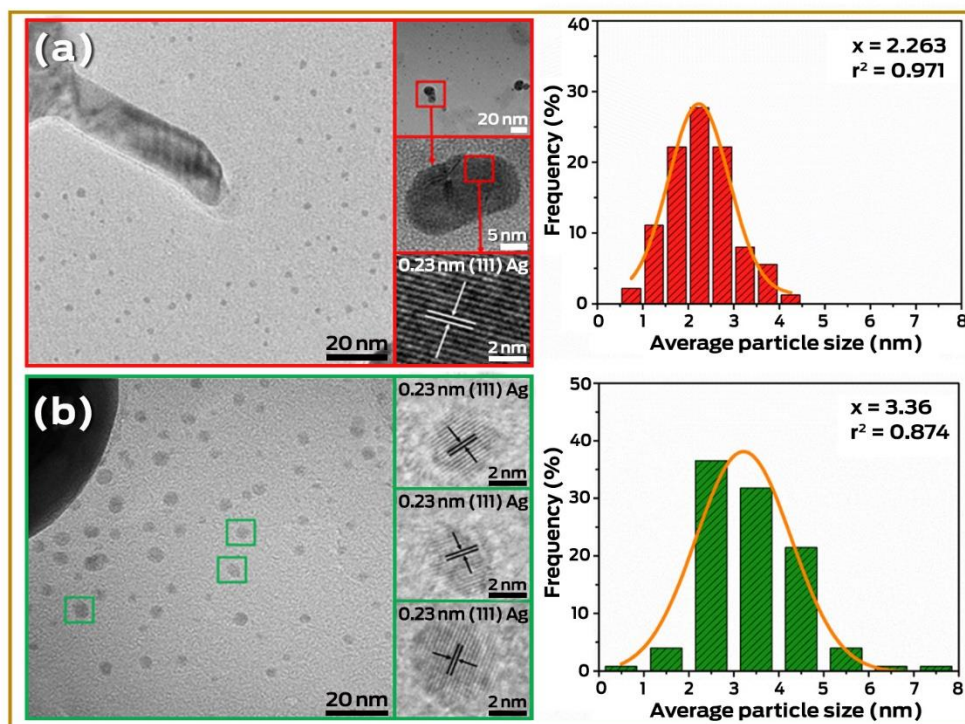


Figure 8. Distribution the particles of Ag° at the Ag_3PO_4 microcrystals with: a) electron irradiation and b) femtosecond laser irradiation

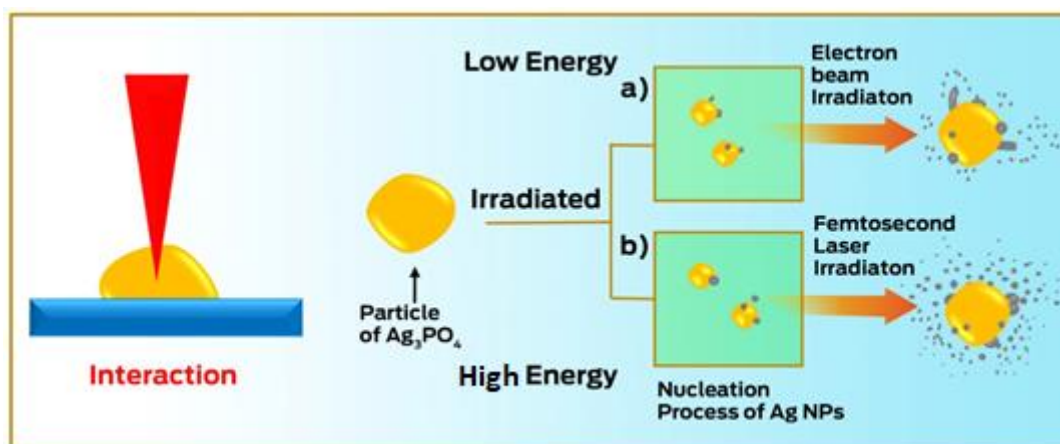


Figure 9. Schematic illustration of the proposed growth mechanism for the formation of metallic Ag on Ag_3PO_4 microcrystals: (A) surface interaction and (B) Coulomb explosion

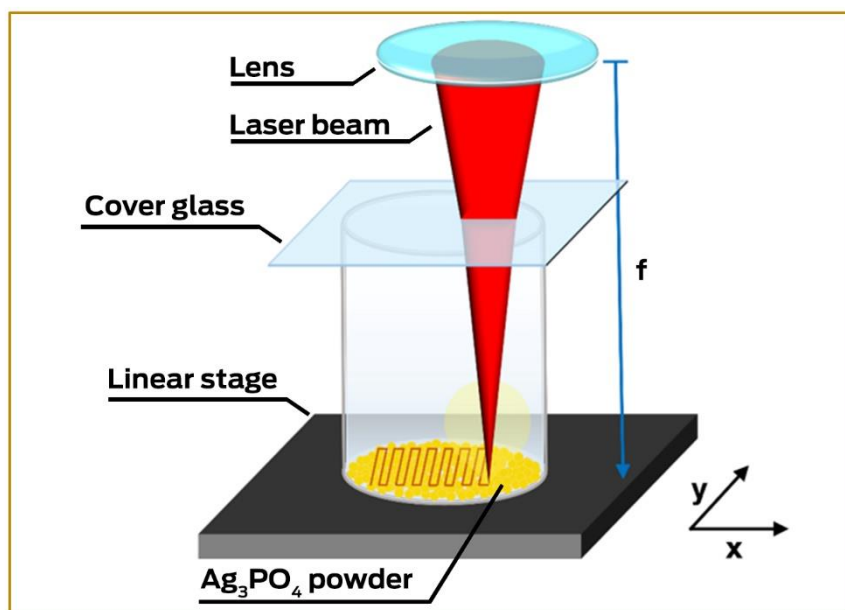


Figure 10. A schematic representation of the experimental procedure for femtosecond laser irradiation.

Table 1. Rietveld refinement details obtained for Ag_3PO_4 microcrystals by the increased replacement of the complex cluster in the lattice

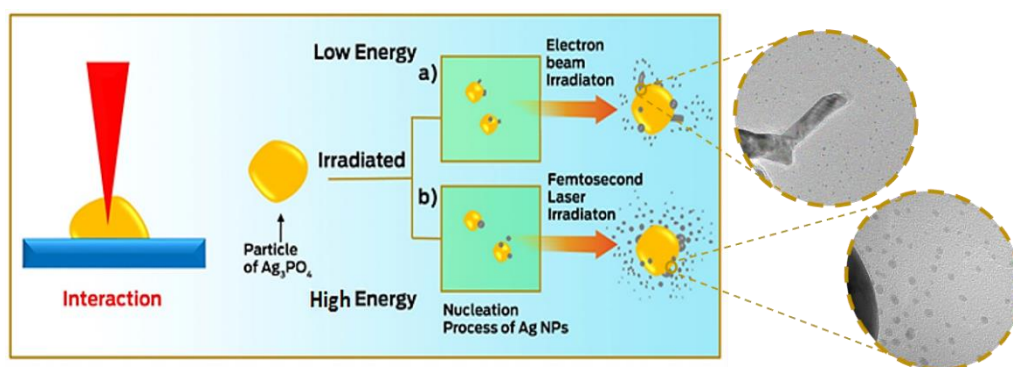
Samples Ag_3PO_4	Lattice Parameters			Cell volume (\AA^3)	R_{Bragg} (%)	χ^2 (%)	R_{wp} (%)	R_{p} (%)
	$\alpha = \beta = \gamma = 90^\circ$							
	a (\AA)	b (\AA)	c (\AA)					
pAP	6.015(66)	6.015(66)	6.015(66)	217.96(6)	0.0580	1.550	0.075	0.054
eAP	6.016(13)	6.016(13)	6.016(13)	217.74(7)	0.0582	2.020	0.081	0.059
lAP	6.013(54)	6.016(13)	6.016(13)	217.46(6)	0.0731	1.400	0.073	0.061
Ag_3PO_4 (ICSD 1530)	6.004(2)	6.004(2)	6.004(2)	216.43	-	-	-	-

In this work, the samples investigated were pure Ag_3PO_4 , Ag_3PO_4 samples irradiated by electrons and laser irradiated. The characterization of the samples is performed by XRD, Rietveld, MEV, MET and EDS refinements. The XRD confirmed that the irradiated surface layer remains crystalline and, according to the EDS analysis, the surface particles are composed mainly of Ag nanoparticles

Keywords: Ag_3PO_4 , femtosecond laser, electron beam, Ag nanoparticles

*Msc. Clayane Carvalho dos Santos^a, Msc. Marcelo de Assis^a, Dr. Thales Rafael Machado^a, Dr. Paula Fabiana dos Santos Pereira^a, Dr. Gladys Minguez-Vega^b, Dr. Eloisa Cordoncillo^c, Dr. Hector Beltran-Mir^c, Dr. Carlos Doñate-Buendía^b, Dr. Juan Andrés^{*d} and Dr. Elson Longo^a*

Proof of concept studies directed towards the formation of metallic Ag nanostructures from Ag_3PO_4 induced by electron beam and femtosecond laser.



Supporting Information

Proof of concept studies directed towards the formation of metallic Ag nanostructures from Ag₃PO₄ induced by electron beam and femtosecond laser:

Msc. Clayane Carvalho dos Santos^a, Msc. Marcelo de Assis^a, Dr. Thales Rafael Machado^a, Dr. Paula Fabiana dos Santos Pereira^a, Dr. Gladys Minguez-Vega^b, Dr. Eloisa Cordoncillo^c, Dr. Hector Beltran-Mir^c, Dr. Carlos Doñate-Buendía^b, Dr. Juan Andrés^{d} and Dr. Elson Longo^a*

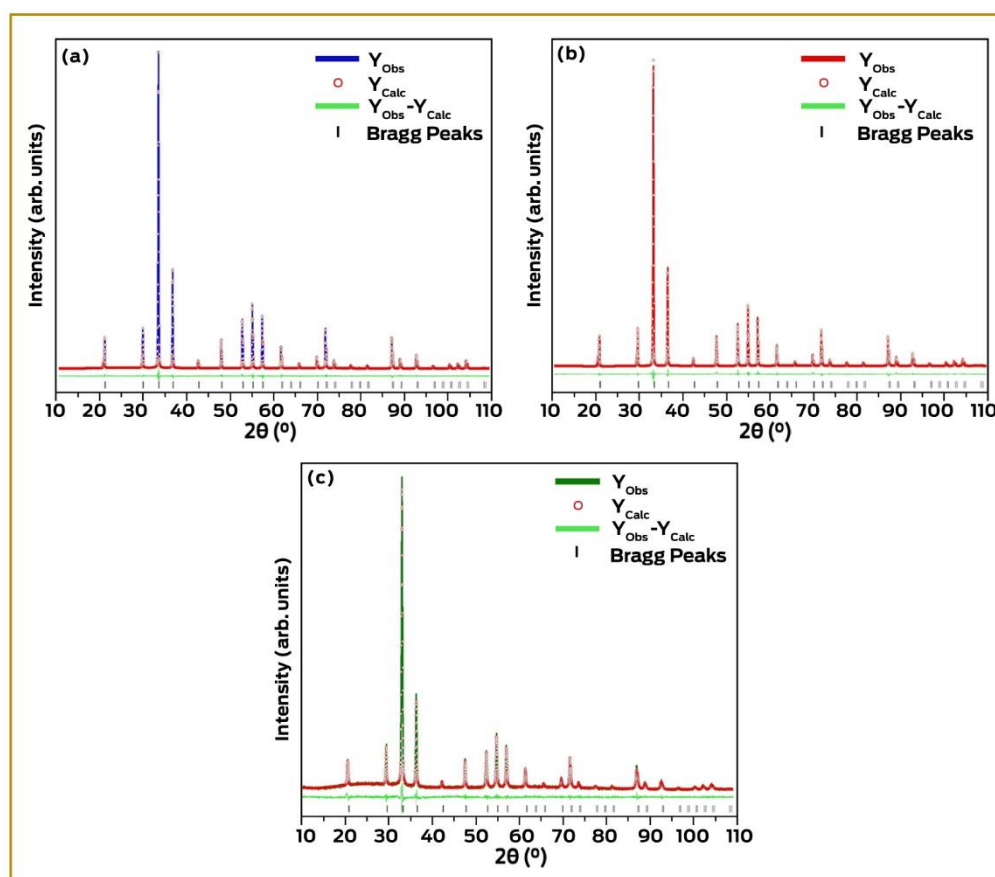


Figure S1: Rietveld refinement plots of Ag₃PO₄ powders obtained by the CP route with: a) pure, b) electron irradiation and c) femtosecond laser irradiation.

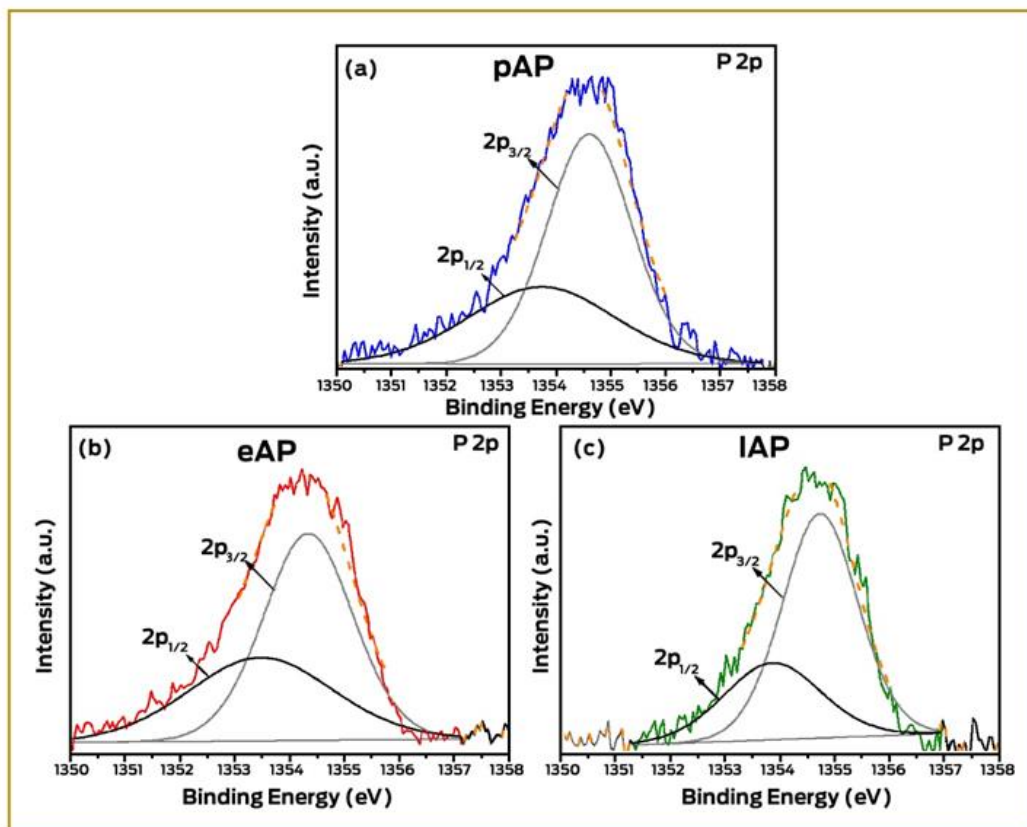


Figure S2: High resolution P 2p XPS spectra of Ag_3PO_4 region of the samples pure (b), electron irradiation (c) and femtosecond laser irradiation.





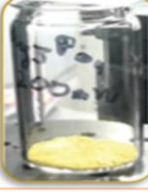
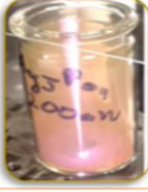
Sample	Power (mW)	The image before starting the irradiation process	Image after ablation
Ag_3PO_4	10		
	80		
	200		

Figure S3: Laser ablation process of femtoseconds at different power values, with: 10, 80 and 200mW.